Journal of Hepatocellular Carcinoma

Dovepress
Taylor & Francis Group

Open Access Full Text Article

ORIGINAL RESEARCH

Intra- and Peritumoral Radiomic Signatures on CECT: Prediction of Aggressive Hepatocellular Carcinoma Subtypes and 2-Year Recurrence

Fengqiu Ruan[1,*], Xuan Li[1,*], Lijuan Feng[1], Shengchen Jiang[1], Zhiming Li[1], Liling Long[1–3]

[1]Department of Radiology, The First Affiliated Hospital of Guangxi Medical University, Nanning, People's Republic of China; [2]Key Laboratory of Early Prevention and Treatment for Regional High Frequency Tumor, Guangxi Medical University, Ministry of Education, Nanning, People's Republic of China; [3]Guangxi Key Laboratory of Immunology and Metabolism for Liver Diseases, Nanning, People's Republic of China

*These authors contributed equally to this work

Correspondence: Liling Long, Department of Radiology, The First Affiliated Hospital of Guangxi Medical University, Nanning, 530000, People's Republic of China, Email cjr.longliling@vip.163.com

Purpose: To evaluate whether radiomic features from contrast-enhanced computed tomography (CECT) of peritumoral regions can be used to preoperatively predict proliferative hepatocellular carcinoma (PHCC).

Patients and Methods: Preoperative CT scans from 486 patients with hepatocellular carcinoma (HCC) were retrospectively analyzed and split into training (n = 252), testing (n = 109), and validation (n = 125) cohorts. Radiomic features were extracted from intra- and peritumoral regions (peri-3 mm, peri-5 mm, and peri-10 mm) on arterial phase (AP) and portal venous phase (PVP) images using PyRadiomics. Features were selected with LASSO regression and 10-fold cross-validation, and a radiomics score (Radscore) was calculated as a weighted sum of selected features. Patients were classified into high- and low-risk groups using the optimal Youden's index cutoff. Recurrence-free survival (RFS) was analyzed with Kaplan–Meier curves, feature contributions were quantified using SHapley Additive exPlanations (SHAP), and model performance was assessed by area under the curve (AUC).

Results: The Naive Bayes model using peri-5 mm features achieved the highest mean AUC (0.739) and accuracy (0.802), with AUCs of 0.839 and 0.639 in internal and external validation. In the test set, combining intra- and peritumoral features improved the AUC to 0.849 (95% CI: 0.773–0.924; sensitivity: 0.974; specificity: 0.606). In the validation set, AP, PVP, and their combined models achieved AUCs of 0.699, 0.672, and 0.695, respectively. SHAP highlighted in the Naive Bayes model that the increased inhomogeneity of the texture grayscale of the peritumoral tissue in the PVP may be associated with more aggressive HCC subtypes. Multivariable analysis identified rim-APHE (OR = 22.667), mosaic architecture (OR = 5.904), and intratumoral hemorrhage (OR = 4.897) as independent risk factors for PHCC (all $p < 0.05$). PHCC showed significantly worse RFS than non-PHCC ($p < 0.0001$). Radscore effectively stratified early recurrence risk ($p < 0.0001$).

Conclusion: Radiomic analysis of intratumoral and peri-5 mm enhancement features enables accurate preoperative PHCC identification and may inform intensified postoperative surveillance and adjuvant therapy.

Keywords: hepatocellular carcinoma, peritumoral radiomics, computed tomography, early recurrence

Introduction

Hepatocellular carcinoma (HCC) is the most prevalent type of primary liver cancer globally, and its incidence continues to rise.[1] Among the numerous HCC subtypes, certain variants exhibit particularly poor prognoses, with higher rates of intrahepatic and extrahepatic metastasis. According to the fifth edition of the World Health Organization (WHO) Classification of Digestive System Tumors,[2] several highly aggressive subtypes have been identified, including the macrotrabecular-massive (MTM), CK19-positive, scirrhous, sarcomatoid, and neutrophil-rich subtypes. Due to their marked aggressiveness, these variants are collectively termed proliferative HCC (PHCC).[3] PHCC is associated with

Received: 24 June 2025
Accepted: 3 December 2025
Published: 21 December 2025

markedly higher postoperative recurrence rates than non-PHCC (NPHCC), and its aggressive biological behavior presents substantial therapeutic challenges.[4]

PHCC is characterized by TP53 mutations and upregulation of angiogenesis-related genes, which contribute to its high aggressiveness and markedly elevated risk of early postoperative recurrence.[5] Early recurrence—defined in several large cohort studies as relapse within 2 years after surgery—often reflects aggressive tumor biology, occult intrahepatic dissemination, or microscopic metastasis.[6,7] Histopathological evidence shows that microvascular invasion (MVI) in HCC frequently extends several millimeters beyond the visible tumor boundary.[8] Accordingly, peritumoral margins of 5–10 mm can be used to detect and characterize MVI and differentiate tumor grade.[9,10] For highly aggressive tumors, surgical resection alone is often insufficient, necessitating adjuvant therapy and close monitoring. Emerging evidence highlights the importance of tumor biology in therapeutic decision-making, particularly regarding angiogenesis patterns. Anti-angiogenic agents such as bevacizumab and lenvatinib have demonstrated enhanced efficacy against hypervascular tumors by suppressing angiogenesis.[11,12] Furthermore, preoperative neoadjuvant therapy can also induce tumor necrosis, reduce proliferative activity, and decrease the risk of postoperative recurrence and metastasis.[13,14]

HCC represents a highly heterogeneous disease, with distinct biological characteristics manifesting in specific temporal and spatial imaging patterns.[15,16] Multiphase contrast-enhanced computed tomography (CECT)—including noncontrast, arterial phase (AP), portal venous phase (PVP), and delayed phase—can capture these features, providing crucial information on tumor blood supply, morphology, and treatment outcomes.[17] Aggressive HCCs frequently exhibit radiological hallmarks such as incomplete capsule formation, rim AP hyperenhancement, and satellite lesions.[18,19] Therefore, the peritumoral region may contain critical information on MVI, tumor–stroma interactions, and early metastatic potential.

Radiomics has emerged as a transformative computational approach in oncologic imaging, enabling the extraction of high-dimensional quantitative features from medical images. However, most existing radiomics studies in HCC have focused primarily on intratumoral features,[17,20] which may inadequately reflect the biological heterogeneity extending beyond the tumor boundaries. In the present study, we systematically compared peritumoral margins of varying extents in PHCC using multiphase computed tomography (CT) radiomics to characterize both tumor and peritumoral heterogeneity. By integrating this underutilized peritumoral information, our approach aims to improve early diagnosis, guide therapeutic strategies, and refine prognostic assessment for patients with PHCC.

Materials and Methods

Patients

This study was approved by the institutional ethics committees at both participating centers (Center 1, The First Affiliated Hospital of Guangxi Medical University, 2025-E0431; Center 2, Guangxi Medical University Cancer Hospital, KY2025984), with a waiver of informed consent due to its retrospective design. Patients with HCC were enrolled from Center 1 between March 2016 and March 2023 and from Center 2 between January and December 2021. Inclusion criteria were:

1. Pathologically confirmed HCC with complete clinical and pathological data.
2. Multi-phase CECT of the liver performed within 1 month prior to surgery.

Exclusion criteria were:

1. Unsatisfactory CT images, such as incomplete scans or severe artifacts obscuring tumor margins.
2. Prior treatment for HCC, including chemotherapy, radiotherapy, transarterial chemoembolization (TACE), or radiofrequency ablation.
3. History of concurrent tumors from other systems or distant metastases before surgery.

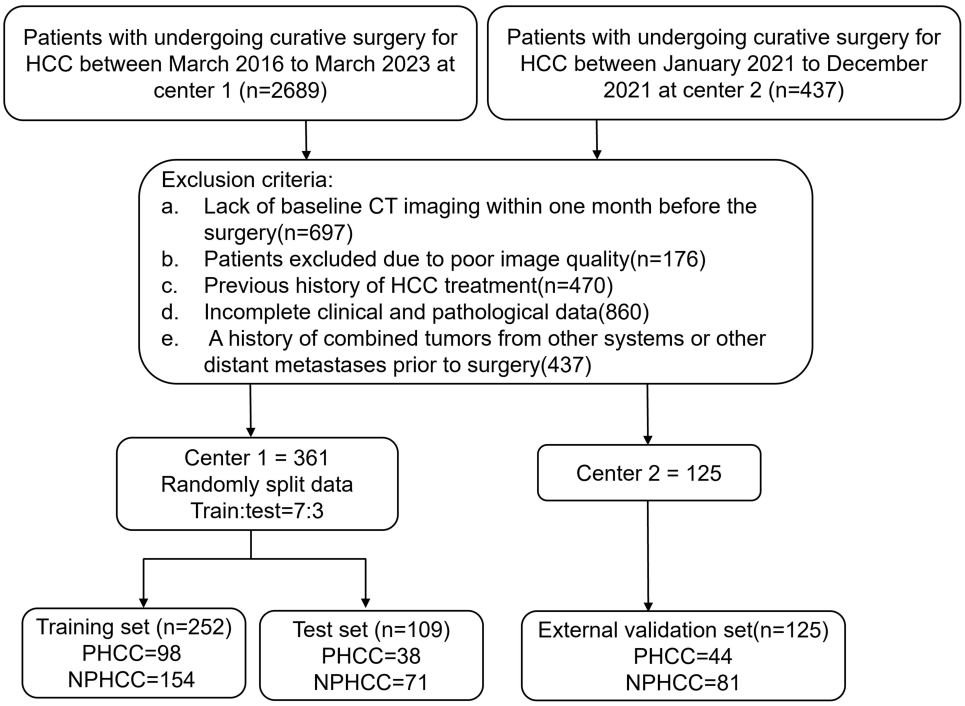

Figure 1 Flowchart for selecting the patients.

A total of 486 patients who underwent radical surgical resection for HCC at the two centers met these criteria and were included in the study (Figure 1).

CT Image Acquisition Protocol

All patients underwent contrast-enhanced abdominal CT using Siemens or GE scanners after a 4–6-hour fast. Scans were acquired at 120 kV with automatic tube current modulation; slice thickness and interval were both 5 mm. The scan range extended from the diaphragmatic dome to the inferior hepatic margin. Following noncontrast scanning, a nonionic iodinated contrast agent (1.3–1.5 mL/kg body weight; total dose 60–110 mL) was administered via the antecubital vein at 3–3.5 mL/s using a power injector. Dynamic contrast-enhanced images were acquired during the AP (25–30 s), PVP (55–60 s), and delayed phase (120 s). For Siemens systems, bolus tracking was performed at the abdominal aorta with a 120 HU trigger threshold, after which the three-phase enhanced scan was initiated. Device-specific acquisition parameters are detailed in Supplementary Table 1.

Laboratory Examinations and Follow-Up

Patient data—including demographic characteristics, preoperative laboratory results, and biochemical profiles—were retrieved from the hospital information system. Detailed baseline indicators are summarized in Table 1.

Postoperative follow-up was performed at 3- to 6-month intervals and included serum alpha-fetoprotein measurements as well as enhanced CT, magnetic resonance imaging (MRI), or ultrasound imaging. For patients who missed scheduled visits, follow-up information was obtained via telephone interviews.

Tumor recurrence was defined as the detection of intrahepatic or extrahepatic lesions on imaging (CT or MRI) or by pathological confirmation. Early recurrence was defined as the appearance of new intrahepatic or extrahepatic lesions within 2 years after surgery. The follow-up endpoint was recurrence-free survival (RFS)—defined as recurrence, metastasis, or death—within the 2-year postoperative period. Patients without these events were censored at their last follow-up date. Follow-up continued until April 2025.

https://doi.org/10.2147/JHC.S549301

Table 1 Baseline Clinical and Radiological Features of the Datasets

Factors	Training Set (n=252)		p	Test Set (n=109)		p	Validation Set (n=125)		p
	NPHCC	PHCC		NPHCC	PHCC		NPHCC	PHCC	
Age (years)	50 ± 11	49 ± 12	0.423	50 ± 11	53 ± 10	0.209	54 ± 11	50 ± 13	0.070
Gender(male)	131(85.06)	81(82.65)	0.610	64(90.14)	33(86.84)	0.749	72(88.89)	35(79.55)	0.155
HBV	133(86.36)	78(79.59)	0.156	61(85.92)	29(76.32)	0.208	75(92.59)	36(81.82)	0.081
Cirrhosis	76(49.35)	26(26.53)	<0.001	37(52.11)	9(23.68)	0.004	55(67.90)	32(72.73)	0.575
Liverfluke	43(27.92)	16(16.33)	0.034	19(26.76)	13(34.21)	0.416	2(2.47)	5(11.36)	0.095
BCLC staging(B&C)	42(27.27)	43(43.88)	0.007	20(28.17)	17(44.74)	0.082	25(30.86)	18(40.91)	0.259
NLR	1.81[1.41, 2.55]	2.52[1.74, 3.44]	<0.001	1.90[1.44, 2.65]	2.69[1.49, 4.73]	0.034	1.88 [1.45, 2.51]	2.06 [1.54, 3.22]	0.224
PLT(10^9/L)	179[136, 231]	219[175, 280]	<0.001	180[136, 220]	244[137, 327]	0.008	167 [141, 202]	214 [166, 270]	0.003
TBil(umol/L)	11[8, 16]	12[8, 17]	0.512	11.1[7.5, 16.1]	11.9[8.0, 15.8]	0.854	13.7[10.4, 17.1]	12.9 [9.9, 17.2]	0.856
ALB(g/L)	39.0[36.0, 41.8]	39.4[36.9, 41.7]	0.518	39.6[37.1, 41.9]	37.9[35.4, 41.1]	0.125	38.6 [36.6, 40.7]	38.5 [36.2, 41.8]	0.867
AST(U/L)	33[25, 44]	38[28, 50]	0.045	32[26, 41]	36[24, 69]	0.240	40 [32, 54]	39 [33, 51]	0.743
ALT(U/L)	33[24, 47]	34[22, 51]	0.856	34[24, 50]	29[18, 54]	0.227	37 [24, 50]	30 [20, 40]	0.027
AFP(≥400mg/mL)	52(33.77)	70(71.43)	<0.001	17(23.94)	24(63.16)	<0.001	23 (28.40)	28(63.64)	<0.001
Tumor size(≥5cm)	52 (33.77)	71 (72.45)	<0.001	19 (26.76)	32 (84.21)	<0.001	33 (40.74)	30 (68.18)	0.003
Irregular shape	50 (32.47)	55 (56.12)	<0.001	25 (35.21)	26 (68.42)	<0.001	33 (40.74)	28 (63.64)	0.014
Satellite nodules	19 (12.34)	24 (24.49)	0.012	9 (12.68)	13 (34.21)	0.008	8 (9.88)	14 (31.82)	0.002
Complete capsule	45 (29.22)	22 (22.45)	0.236	24 (33.80)	9 (23.68)	0.273	27 (33.33)	2 (4.55)	<0.001
Peritumoral enhancement	28 (18.18)	29 (29.59)	0.035	15 (21.13)	13 (34.21)	0.136	8 (9.88)	13 (29.55)	0.005
Progressive enhancement	6 (3.90)	12 (12.24)	0.012	2 (2.82)	3 (7.89)	0.340	4 (4.94)	0 (0.00)	0.297
Intratumoral hemorrhage	21 (13.64)	38 (38.78)	<0.001	10 (14.08)	15 (39.47)	0.003	9 (11.11)	11 (25.00)	0.043
Intratumoral fat	10 (6.49)	6 (6.12)	0.906	5 (7.04)	2 (5.26)	>0.999	9 (11.11)	0 (0.00)	0.026
Rim-APHE	2 (1.30)	14 (14.29)	<0.001	2 (2.82)	5 (13.16)	0.049	1 (1.23)	9 (20.45)	<0.001
Non-rim-APHE	106 (68.83)	58 (59.18)	0.117	46 (64.79)	27 (71.05)	0.508	61 (75.31)	29 (65.91)	0.264
Intratumoral necrosis	78 (50.65)	79 (80.61)	<0.001	38 (53.52)	33 (86.84)	<0.001	51 (62.96)	35 (79.55)	0.056
Intratumoral arteries	83 (53.90)	76 (77.55)	<0.001	37 (52.11)	33 (86.84)	<0.001	40 (49.38)	34 (77.27)	0.002
Mosaic architecture	6 (3.90)	21 (21.43)	<0.001	2 (2.82)	9 (23.68)	0.001	0 (0.00)	4 (9.09)	0.014
Nodule-in-nodule	7 (4.55)	6 (6.12)	0.581	8 (11.27)	3 (7.89)	0.744	4 (4.94)	2 (4.55)	>0.999
PVP hyperenhancement	44 (28.57)	11 (11.22)	0.001	18 (25.35)	5 (13.16)	0.137	6 (7.41)	1 (2.27)	0.420
PVP non-peripheral washout	64 (41.56)	60 (61.22)	0.002	29 (40.85)	28 (73.68)	0.001	57 (70.37)	35 (79.55)	0.266

Notes: Define the maximum diameter of the tumor as the tumor size (centimeter). For continuous variables, the mean ± SD is expressed in () if the variable is normally distributed, otherwise the median and IQR are expressed in []. Categorical variables are shown as proportions (%); the % symbol is omitted from table cells for brevity.

Abbreviations: Rim-APHE, Rim arterial phase hyperenhancement; HBV, Hepatitis B Virus; AFP, Alpha-fetoprotein; ALT, Alanine Aminotransferase; AST, Aspartate Aminotransferase; TBil, Total Bilirubin; BCLC, Barcelona Clinic Liver Cancer; NLR, Neutrophil-to-Lymphocyte Ratio; PLT, Platelet Count; ALB, Albumin; PVP, Portal venous phase.

Histopathologic Analysis

All patients underwent histopathologic evaluation after hepatectomy, and complete pathology reports were available. According to the fifth edition of the WHO classification of Digestive System Tumors, PHCC subtypes included: (1) CK19-positive HCC (> 5% positivity), (2) MTM-HCC (> 10 cell layers), (3) sarcomatoid HCC, (4) neutrophil-rich HCC, and (5) scirrhous HCC. NPHCC subtypes included: (1) CK19-negative HCC, (2) clear-cell HCC, (3) steatohepatitic HCC, and (4) lymphocyte-rich HCC.

Radiomics Analysis

Region of Interest (ROI) Segmentation and Peritumoral Expansion

Liver CT images for all patients were exported in DICOM format from the Picture Archiving and Communication System. Preprocessing included standardized display settings (window width, 250 HU; window level, 50 HU) to optimize lesion conspicuity and isotropic voxel resampling ($1 \times 1 \times 1\ mm^3$) to ensure spatial uniformity across the dataset.

Two experienced radiologists, blinded to the patients' clinical and pathological data, independently performed slice-by-slice manual segmentation of the ROIs on AP and PVP images using ITK-SNAP (version 3.8.0; http://www.itksnap.org). For patients with multiple lesions, the largest lesion was selected for volumetric analysis. Peritumoral regions were generated by automatically expanding the tumor boundary by 3 mm, 5 mm, and 10 mm. Interfering structures, such as large blood vessels or bile ducts, were excluded using the "clear label" tool.

To assess reproducibility, 30 cases from each of the AP and PVP images were randomly selected for re-segmentation 3 months later. Inter- and intra-observer reproducibility of radiomic features was evaluated using intraclass correlation coefficients (ICCs); features with ICCs ≥ 0.75 were considered highly reliable; however, those with ICCs < 0.75 were excluded. Discrepancies were resolved through consultation with a senior abdominal radiologist. The imaging radiomics analysis workflow is shown in Figure 2.

Feature Extraction

Handcrafted radiomic features were extracted using Pyradiomics (http://pyradiomics.readthedocs.io) and categorized as geometric, intensity, and texture features. Geometric features quantified three-dimensional tumor shape properties; in contrast, intensity features captured the first-order statistical distribution of voxel intensities. Texture features described higher-order spatial relationships and were computed using the following matrices: gray-level dependence matrix (GLDM), gray-level co-occurrence matrix (GLCM), gray-level run-length matrix (GLRLM), gray-level size zone matrix (GLSZM), and neighboring gray-tone difference matrix (NGTDM). Features were extracted from both intratumoral regions and three peritumoral regions (peri-3 mm, peri-5 mm, peri-10 mm) in the AP and PVP. The same extraction procedures were applied to peritumoral regions as to intratumoral regions.

Feature Selection

All radiomic features underwent statistical and computational screening to optimize model performance. First, features were standardized using Z-score normalization ($z = (x - \mu)/\sigma$) to reduce scale-related bias. Highly correlated features (Spearman correlation coefficient > 0.9) were filtered, retaining only one from each correlated set. Dimensionality reduction was then performed using the least absolute shrinkage and selection operator (LASSO) regression (Figure 3). Ten-fold cross-validation was used to identify the optimal regularization parameter λ by minimizing the mean cross-validation error. Feature selection was performed separately for each phase, and retained features were concatenated for joint classification, thereby leveraging complementary information from both enhancement phases. Each patient's radiomics score (Radscore) was calculated as a weighted linear combination of the retained features. LASSO regression modeling was implemented using Python's scikit-learn library, with features exhibiting nonzero coefficients included in model fitting and combined into a radiomics signature. Four machine-learning algorithms—Naive Bayes (NB), Random Forest (RF), Light Gradient Boosting Machine (LightGBM), and Extremely Randomized Trees (Extra Trees)—were implemented using the scikit-learn library and LightGBM packages. To optimize model performance, hyperparameter tuning was conducted using grid search combined with 10-fold cross-validation on the training cohort. Specific information on parameter optimization is provided in Appendix A1.

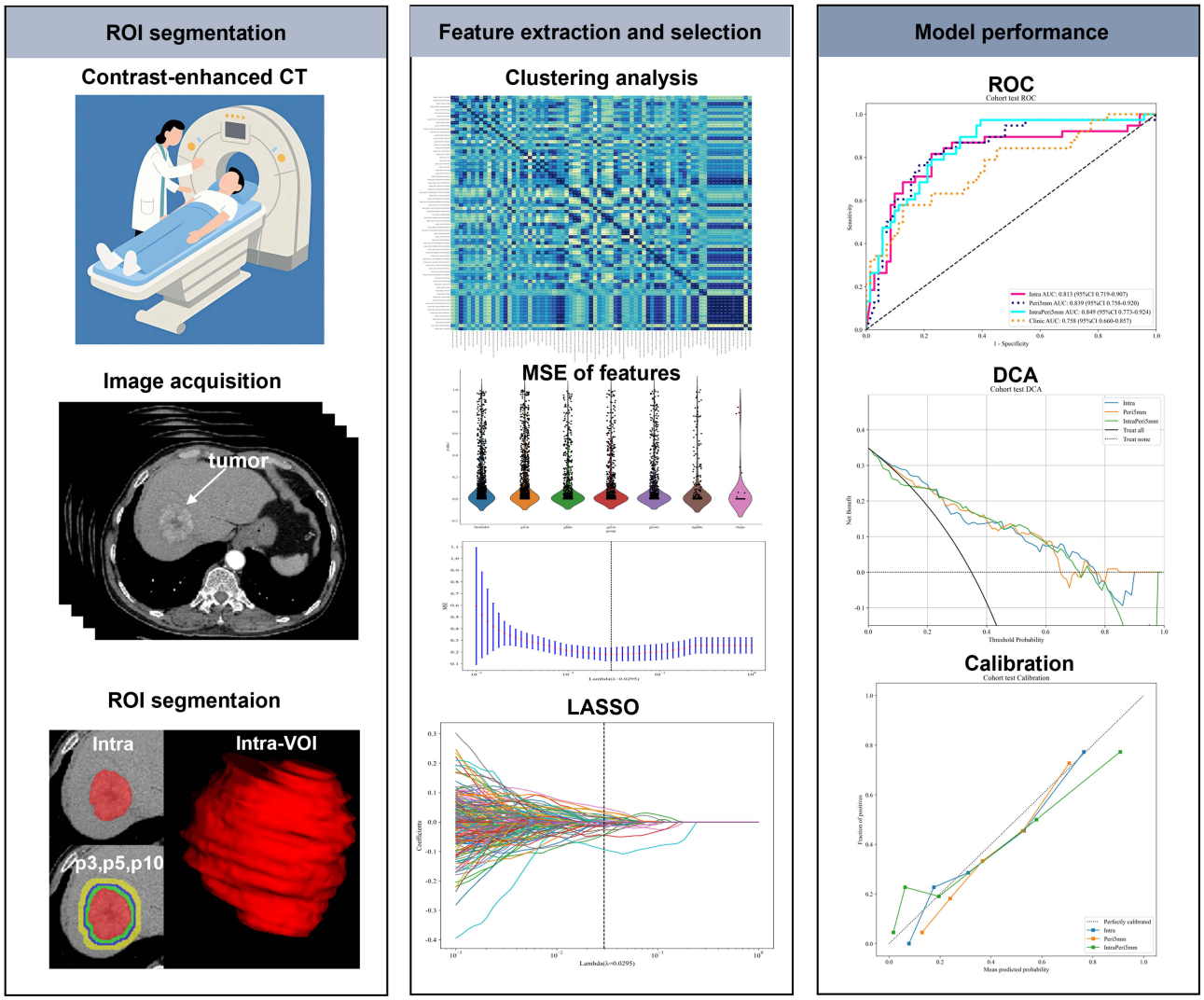

Figure 2 Radiomics analysis workflow.

Radiomics Signature

The features from intratumoral and peritumoral regions were subjected to LASSO-based selection to identify the most informative predictors. A feature-level fusion strategy was applied to integrate AP and PVP features from each region, and the prediction probabilities of the three peritumoral models (peri-3 mm, peri-5 mm, peri-10 mm) were compared. The best-performing model was then combined with the intratumoral model to generate an integrated intra-peritumoral fusion model (IntraPeri). Ten-fold cross-validation was applied to develop the final imaging model and determine the optimal classifier. Model outputs were visualized using SHapley Additive exPlanations (SHAP), a game-theoretic approach for quantifying each feature's contribution to the model's predictions.

The diagnostic performances of each radiomics model was evaluated using receiver operating characteristic (ROC) analysis. The model with the highest area under the curve (AUC) was considered optimal. Model performance was further assessed using specificity, sensitivity, Youden's index, AUC, and the F1 score, which incorporates both precision and recall. The research design adheres to the Radiomics Quality Score (RQS) standards to ensure the rigor and reproducibility of the research (Appendix A2).

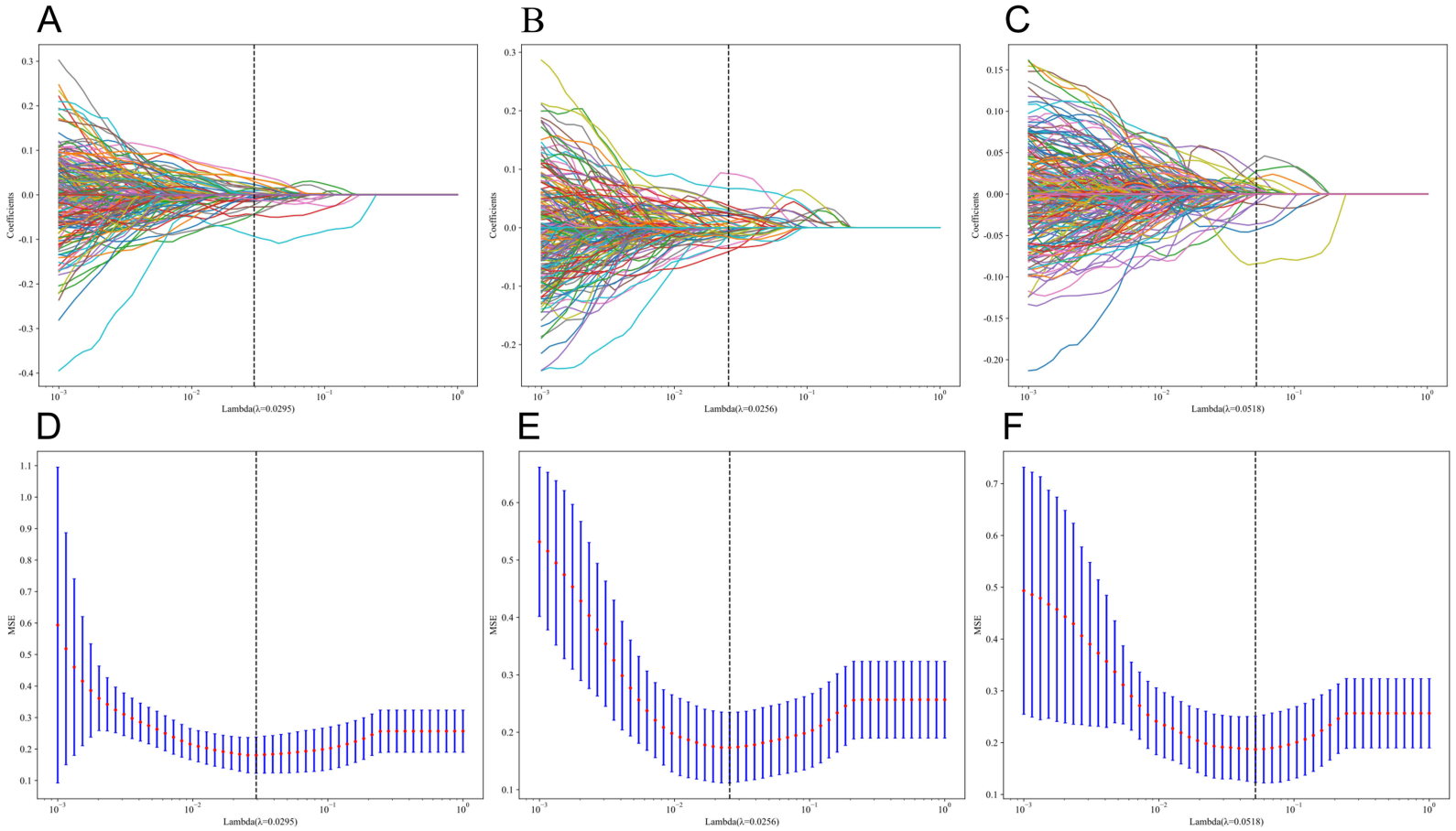

Figure 3 Feature selection for radiomics. (**A**–**C**) LASSO coefficient profiles across different λ values; vertical dashed lines indicate the number of features corresponding to the optimal λ. (**D**–**F**) Optimal λ values selected by 10-fold cross-validation with minimum MSE, shown by vertical dashed lines. Panels represent intratumoral (**A** and **D**), peritumoral (**B** and **E**) and fused features (**C** and **F**).
Abbreviation: MSE, mean squared error.

Clinical-Radiological Model Construction

Contrast-enhanced CT images were analyzed to assess both intra- and peritumoral features of HCC. Evaluated characteristics included tumor size, irregular shape, presence of satellite nodules, capsule integrity, peritumoral enhancement, and progressive enhancement. Intratumoral findings encompassed hemorrhage, fat, necrosis, intratumoral arteries, mosaic architecture, and nodule-in-nodule appearance. Enhancement patterns were also assessed, including rim AP hyperenhancement (rim-APHE), non-rim APHE, PVP hyperenhancement, and PVP non-peripheral washout. All imaging features were independently evaluated by two experienced abdominal radiologists, with discrepancies resolved by consensus. The definition of CT radiological features is provided in the Supplementary Table 2. Inter-observer agreement for qualitative CT features was assessed using Cohen's kappa coefficient. The clinical and qualitative CT features were first analyzed using univariable analysis, and variables showing statistical significance were subsequently entered into multivariable logistic regression to identify independent clinico-radiological predictors.

Statistical Analysis

Baseline clinical characteristics were analyzed using t tests, chi-square tests, or Fisher's exact tests in SPSS software (version 25.0, IBM). Continuous variables were presented as mean ± standard deviation for normally distributed data or median (interquartile range) for non-normally distributed data. Categorical variables were compared using chi-square or Fisher's exact tests. Radiomics features were screened with the Mann–Whitney *U*-test, retaining only those with $p < 0.05$. The ICC analysis, the DeLong test, and the Hosmer–Lemeshow test were performed using R software (version 4.2.3). Spearman rank correlation analysis, Z-score normalization, LASSO regression, and ROC curve plotting were conducted using Python (version 3.7.17; http://www.python.org). A two-tailed p-value < 0.05 was considered statistically significant. According to standard statistical guidelines (Peduzzi et al),[21] sample size adequacy was assessed via the EPV ratio. With 98 PHCC events in the training cohort and 7 independent predictors included in the final multivariable analysis, the calculated EPV was 14.0. This exceeds the standard threshold of 10, indicating robust statistical power relative to the model complexity.

Results

Baseline Characteristics of Patients

A total of 486 patients with HCC were included in this study, comprising 180 cases of PHCC and 306 cases of NPHCC; the detailed subtype distribution is shown in Figure 1. Patients from the primary cohort were randomly assigned to training and testing cohorts in a 7:3 ratio, with the external cohort reserved for validation. Clinical and imaging characteristics of the training, testing, and validation cohorts are summarized in Table 1. No significant differences in age or sex were observed between the PHCC and NPHCC groups across the three datasets (all $p > 0.05$). Multivariable analysis identified cirrhosis (odds ratio [OR]: 0.241, 95% confidence interval [CI]: 0.135–0.430), liver fluke infection (OR: 0.395, 95% CI: 0.202–0.771), intratumoral hemorrhage (OR: 4.897, 95% CI: 2.601–9.217), rim-APHE (OR: 22.667, 95% CI: 4.909–104.690), PVP hyperenhancement (OR: 0.317, 95% CI: 0.152–0.660), and mosaic architecture (OR: 5.904, 95% CI: 2.342–14.895) as independent predictors of PHCC ($p < 0.05$; Table 2).

Table 2 Univariable and Multivariable Analysis of Clinical-Radiological Features

Features	Univariable Analysis		Multivariable Analysis	
	OR (95% CI)	p	OR (95% CI)	p
Age	0.991(0.987, 0.995)	<0.001	0.989(0.970, 1.009)	0.358
Gender(male)	0.618(0.490, 0.780)	0.001	1.072(0.518, 2.219)	0.874
HBV	0.586(0.464, 0.742)	<0.001	1.026(0.510, 2.065)	0.952
Cirrhosis	0.342(0.236, 0.497)	<0.001	0.241(0.135, 0.430)	<0.001
Liverfluke	0.372(0.230, 0.602)	0.001	0.395(0.202, 0.771)	0.022
AFP(≥400mg/mL)	1.346(0.996, 1.818)	0.104		

(*Continued*)

Table 2 (Continued).

Features	Univariable Analysis		Multivariable Analysis	
	OR (95% CI)	p	OR (95% CI)	p
BCLC(B&C)	1.024(0.717, 1.462)	0.914		
ALT	0.994(0.990, 0.998)	0.01	0.999(0.994, 1.004)	0.674
AST	0.997(0.993, 1.000)	0.124		
TBiL	0.992(0.983, 1.002)	0.174		
ALB	0.988(0.983, 0.994)	<0.001	1.010(0.977, 1.044)	0.621
PLT	0.999(0.998, 1.000)	0.054		
NLR	0.946(0.899, 0.995)	0.073		
Tumor size(≥5cm)	1.365(1.011, 1.844)	0.088		
Complete capsule	0.489(0.319, 0.750)	0.006	0.544(0.292, 1.013)	0.107
Nodule in nodule	0.857(0.343, 2.140)	0.782		
Irregular shape	1.100(0.798, 1.517)	0.626		
Satellite nodules	1.263(0.763, 2.094)	0.447		
Intratumoral hemorrhage	1.810(1.157, 2.829)	0.029	4.897(2.601, 9.217)	<0.001
Intratumoral arteries	0.916(0.705, 1.189)	0.579		
Intratumoral necrosis	1.013(0.779, 1.317)	0.936		
Intratumoral fat	0.600(0.257, 1.404)	0.323		
Rim-APHE	7.000(2.02, 24.264)	0.01	22.667(4.909, 104.69)	0.001
Non-rim-APHE	0.547(0.418, 0.716)	<0.001	0.982(0.550, 1.752)	0.959
PVP hyperenhancement	0.250(0.144, 0.435)	<0.001	0.317(0.152, 0.660)	0.01
PVP non peripheral washout	0.938(0.698, 1.260)	0.719		
Peritumoral enhancement	1.036(0.670, 1.602)	0.895		
Mosaic architecture	3.500(1.634, 7.493)	0.007	5.904(2.342, 14.895)	0.002
Progressive enhancement	2.000(0.879, 4.554)	0.166		

Abbreviations: Rim-APHE, Rim arterial phase hyperenhancement; PVP, Portal venous phase.

Model Performance Evaluation and Comparison

The average ICCs for tumor boundary delineation between and within observers were 0.8 and 0.85, respectively, indicating satisfactory reproducibility of feature extraction (Figure 4).

From the AP and PVP images of each patient, seven categories comprising 3668 handcrafted features were extracted: 720 first-order features, 28 shape features, and 2920 texture features (GLCM = 880, GLDM = 560, GLRLM = 640,

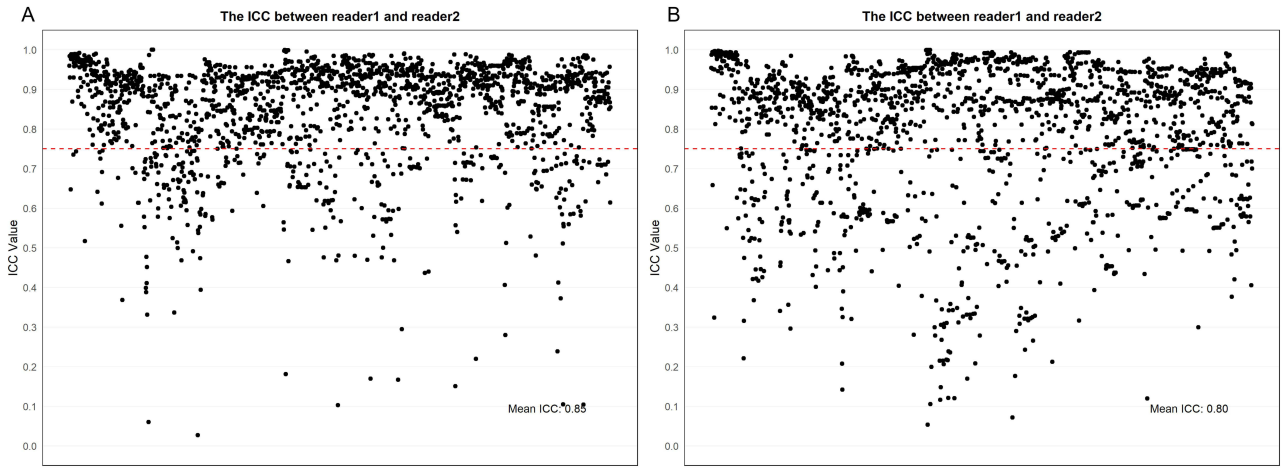

Figure 4 Intraclass correlation coefficient (**A**) and interclass correlation coefficient (**B**). The red line denotes ICCs = 0.75.

https://doi.org/10.2147/JHC.S549301

GLSZM = 640, NGTDM = 200). After fusing the two-phase features and applying Z-score normalization, 2677 features remained. Spearman correlation analysis identified 2211 highly collinear features ($|r| > 0.9$), which were removed. Optimization analysis (Figure 3) was used to determine the optimal penalty coefficient for LASSO regression ($\lambda = 0.0295$), resulting in the selection of 28 significant features from the remaining 466. These features were used to develop the Intratumoral Model.

Radiomics models were compared using four machine-learning algorithms: NB, RF, ET, and LightGBM. The intratumoral radiomics model demonstrated strong diagnostic performance for predicting the proliferative subtype of HCC, with AUC values of 0.813, 0.814, 0.799, and 0.790 in the test sets, respectively. Radiomics models incorporating peritumoral features at 3 mm, 5 mm, and 10 mm achieved higher AUC values of 0.828, 0.839, and 0.812, respectively. Among the three peritumoral boundaries (peri-3 mm, peri-5 mm, peri-10 mm), the 5-mm region (peri-5 mm) yielded the highest testing performance. The NB classifier achieved the highest predictive accuracy for PHCC in the peri-5 mm cohort (AUC: 0.839, 95% CI: 0.758–0.920; sensitivity: 0.763; specificity: 0.817). Consequently, the 5-mm peritumoral boundary was selected for integration into the final intratumoral–peritumoral fusion model. Detailed performance metrics are presented in Table 3.

The fusion model integrating intratumoral and optimal peritumoral (5 mm) radiomic features demonstrated robust performance, as evidenced by AUC values in both the training and test sets (Table 4). Multi-phase analysis revealed that

Table 3 Comparison of Algorithms Across Different Peritumoral Regions

	AUC	95% CI	SEN	SPE	PPV	NPV	F1	Task
Peri3mm								
NB	0.894	0.8538–0.9336	0.888	0.779	0.719	0.916	0.795	Train
NB	0.748	0.6429–0.8530	0.684	0.775	0.619	0.821	0.65	Test
NB	0.629	0.5093–0.7477	0.477	0.926	0.778	0.765	0.592	Val
RF	0.933	0.9046–0.9622	0.898	0.818	0.759	0.926	0.822	Train
RF	0.782	0.6946–0.8699	0.842	0.662	0.571	0.887	0.681	Test
RF	0.628	0.5173–0.7381	0.523	0.765	0.548	0.747	0.548	Val
ET	0.901	0.8621–0.9407	0.908	0.799	0.742	0.932	0.817	Train
ET	0.828	0.7507–0.9058	0.842	0.69	0.593	0.891	0.696	Test
ET	0.685	0.5806–0.7895	0.659	0.716	0.558	0.795	0.604	Val
LGBM	0.948	0.9230–0.9734	0.929	0.877	0.827	0.951	0.875	Train
LGBM	0.780	0.6884–0.8720	0.868	0.606	0.541	0.896	0.667	Test
LGBM	0.582	0.4770–0.6880	0.795	0.370	0.407	0.769	0.538	Val
Peri5mm								
NB	0.889	0.8489–0.9301	0.857	0.825	0.757	0.901	0.804	Train
NB	0.839	0.7578–0.9197	0.763	0.817	0.69	0.866	0.725	Test
NB	0.639	0.5266–0.75009	0.568	0.815	0.625	0.776	0.595	Val
RF	0.937	0.9089–0.9657	0.908	0.857	0.802	0.936	0.852	Train
RF	0.813	0.7307–0.8957	0.816	0.704	0.596	0.877	0.689	Test
RF	0.634	0.5314–0.7368	0.818	0.420	0.434	0.810	0.567	Val
ET	0.899	0.8607–0.9363	0.888	0.805	0.744	0.919	0.809	Train
ET	0.836	0.7609–0.9114	0.842	0.746	0.64	0.898	0.727	Test
ET	0.639	0.5299–0.7476	0.523	0.802	0.590	0.756	0.590	Val
LGBM	0.946	0.9195–0.9722	0.949	0.838	0.788	0.963	0.861	Train
LGBM	0.800	0.7136–0.8858	0.605	0.887	0.742	0.808	0.667	Test
LGBM	0.620	0.5121–0.7272	0.545	0.741	0.533	0.545	0.539	Val
Peri10mm								
NB	0.882	0.8400–0.9237	0.908	0.721	0.674	0.925	0.774	Train
NB	0.768	0.6664–0.8688	0.711	0.831	0.692	0.843	0.701	Test
NB	0.625	0.5169–0.7328	0.523	0.778	0.561	0.750	0.541	Val
RF	0.936	0.9088–0.9630	0.847	0.864	0.798	0.899	0.822	Train
RF	0.812	0.7275–0.8959	0.868	0.69	0.600	0.907	0.71	Test
RF	0.622	0.5148–0.7288	0.500	0.728	0.500	0.500	0.500	Val

(*Continued*)

Table 3 (Continued).

	AUC	95% CI	SEN	SPE	PPV	NPV	F1	Task
ET	0.907	0.8709–0.9423	0.898	0.805	0.746	0.925	0.815	Train
ET	0.789	0.6985–0.8804	0.868	0.676	0.589	0.906	0.702	Test
ET	0.600	0.4935–0.7057	0.682	0.506	0.429	0.745	0.526	Val
LGBM	0.954	0.9311–0.9776	0.929	0.877	0.827	0.951	0.875	Train
LGBM	0.793	0.7000–0.8863	0.658	0.915	0.806	0.833	0.725	Test
LGBM	0.601	0.4964–0.7053	0.545	0.691	0.490	0.737	0.516	Val
Intra								
NB	0.889	0.8475–0.9311	0.888	0.805	0.744	0.919	0.809	Train
NB	0.813	0.7195–0.9073	0.816	0.775	0.66	0.887	0.729	Test
NB	0.669	0.5671–0.7707	0.659	0.691	0.537	0.789	0.592	Val
RF	0.932	0.9037–0.9599	0.878	0.831	0.768	0.914	0.819	Train
RF	0.814	0.7340–0.8946	0.711	0.803	0.659	0.838	0.684	Test
RF	0.693	0.5940–0.7912	0.750	0.630	0.524	0.823	0.617	Val
ET	0.897	0.8598–0.9346	0.888	0.766	0.707	0.915	0.787	Train
ET	0.799	0.7097–0.8874	0.737	0.803	0.667	0.851	0.700	Test
ET	0.689	0.5890–0.7889	0.682	0.679	0.536	0.797	0.6	Val
LGBM	0.949	0.9240–0.9734	0.908	0.87	0.817	0.937	0.86	Train
LGBM	0.790	0.7041–0.8756	0.789	0.718	0.6	0.864	0.682	Test
LGBM	0.699	0.6019–0.7965	0.614	0.765	0.587	0.785	0.600	Val

Abbreviations: AUC, Area under the ROC curve; SEN, Sensitivity; SPE, Specificity; PPV, Positive predictive value; NPV, Negative predictive value; F1, F1 score; CI, Confidence interval; NB, Naive Bayes, RF, Random Forest, ET, Extra Trees, LGBM, LightGBM.

combining AP and PVP features improved test set performance across all fusion models compared with single-phase models. Similarly, the NB classifier achieved the highest predictive accuracy within the fusion model (AUC = 0.849). Feature selection yielded 9 intratumoral signatures (AP: 5; PVP: 4) and 12 peritumoral signatures (AP: 5; PVP: 7). Features with nonzero coefficients were used to construct the intratumoral–peritumoral fusion model, detailed Radscore formulas for the models are provided in Appendix A. SHAP analysis was used to provide a quantitative interpretation of the NB model. As shown in Figure 5, the GLSZM texture feature during the PVP phase (peri_exponential_glszm_GrayLevelNonUniformity_V) was the most important predictor for distinguishing PHCC. High values indicate uneven gray-scale distribution around the tumor, promoting the prediction of high risk and suggesting heterogeneity of the microenvironment.

Clinico-Radiological Model Development and Evaluation

Inter-observer agreement for the assessed radiological features was substantial to excellent, with kappa values ranging up to 0.788. Univariable and multivariable analyses of clinical and radiological characteristics for predicting PHCC in the training cohort are summarized in Table 2. Multivariable logistic regression analysis identified intratumoral hemorrhage, rim-APHE, and mosaic architecture as independent risk factors for PHCC. As shown in Figure 6, in the testing cohort, the AP and PVP fusion model of Intra-peri 5mm maintained robust predictive ability with an AUC of 0.849 (95% CI: 0.773–0.924), which was comparable to that of the combined model (AUC: 0.841, 95% CI: 0.756–0.926) and superior to the clinical model (AUC: 0.741, 95% CI: 0.638–0.843). The DCA curves again demonstrated that the combined and Intra-peri 5mm models provided higher clinical net benefit than the clinical model. Calibration analysis in the testing set also supported favorable agreement between predicted and actual probabilities, particularly for the combined model.

Recurrence-Free Survival (RFS) Analysis

All enrolled patients underwent standardized monitoring for early recurrence over a 2-year postoperative period. Of an initial cohort of 486 eligible cases, 45 patients (PHCC: 18; NPHCC: 27) were excluded due to missing postoperative surveillance data. Within 24 months, 215 recurrence events occurred, yielding an overall recurrence rate of 48.75% (215/

Table 4 Model Performance After Fusion of AP and PVP Using Different Algorithms

IntraPeri5mm	AUC (95% CI)			Cohort
	AP	PVP	A+V	
NB	0.897(0.858–0.937)	0.869(0.824–0.914)	0.890(0.848–0.932)	Train
	0.839(0.760–0.918)	0.838(0.757–0.919)	0.849(0.773–0.924)	Test
	0.699(0.580–0.801)	0.672(0.536–0.752)	0.695(0.591–0.799)	Val
RF	0.929(0.896–0.962)	0.921(0.888–0.953)	0.928(0.897–0.958)	Train
	0.785(0.697–0.873)	0.800(0.716–0.883)	0.836(0.761–0.910)	Test
	0.727(0.628–0.825)	0.684(0.584–0.785)	0.703(0.601–0.804)	Val
ET	0.901(0.865–0.937)	0.881(0.840–0.922)	0.891(0.851–0.931)	Train
	0.807(0.721–0.893)	0.789(0.691–0.887)	0.822(0.744–0.900)	Test
	0.620(0.508–0.732)	0.683(0.585–0.781)	0.678(0.580–0.776)	Val
LGBM	0.950(0.926–0.974)	0.939(0.911–0.966)	0.943(0.917–0.969)	Train
	0.750(0.658–0.842)	0.784(0.699–0.869)	0.801(0.718–0.884)	Test
	0.650(0.542–0.757)	0.657(0.556–0.759)	0.701(0.602–0.801)	Val

Abbreviations: AP, Arterial phase; PVP, Portal venous phase; NB, Naive Bayes; RF, Random Forest; ET, Extra Trees; LGBM, LightGBM.

441), including 54 cases with distant metastasis. The PHCC subtype demonstrated a significantly higher early recurrence rate compared with NPHCC (69.14% vs 36.92%, $p < 0.0001$). Patients were stratified into high-risk and low-risk groups based on Radscore. The optimal cut-off value was determined by maximizing the Youden index (sensitivity + specificity − 1), typically corresponding to the top-left corner of the ROC curve, representing the point with the greatest combined sensitivity and specificity. As shown in Figure 7, the median RFS for the PHCC cohort was 15 months. Overall, the high-risk group exhibited significantly shorter RFS than the low-risk group, consistent with outcomes observed in histologically confirmed PHCC cases.

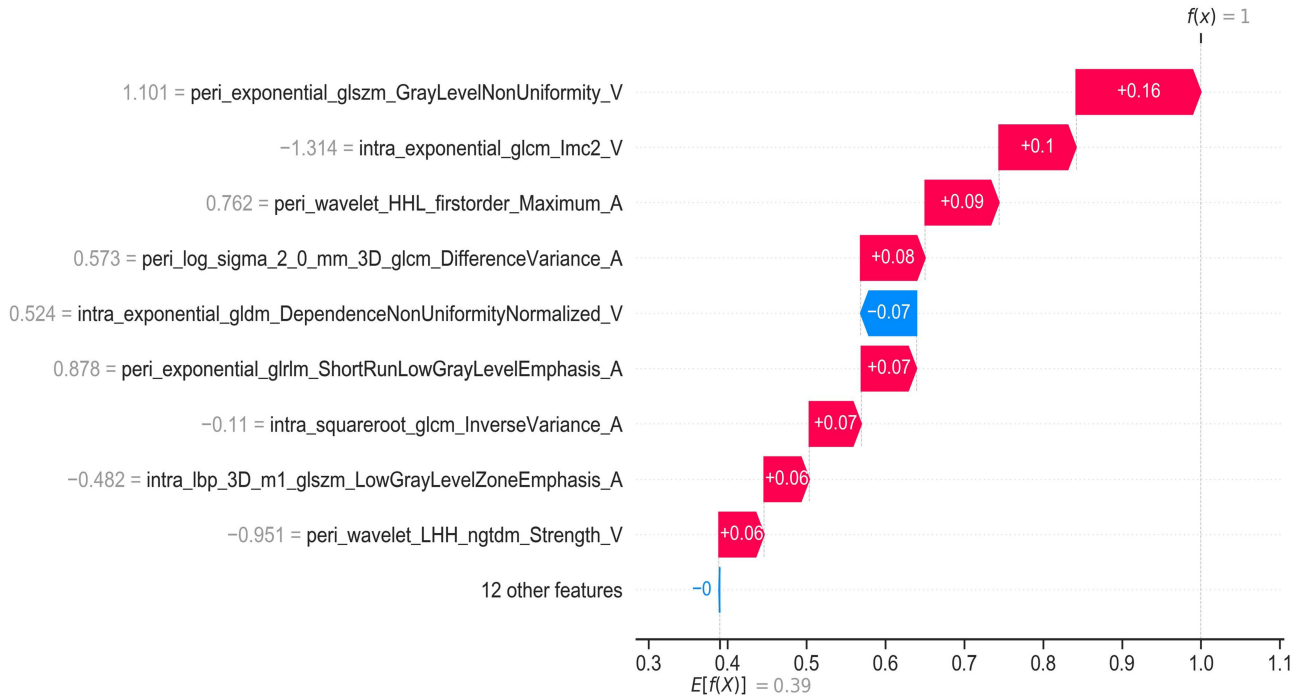

Figure 5 SHAP Waterfall Plot for the Naive Bayes Model.
Abbreviations: A, arterial phase; V, Portal venous phase.

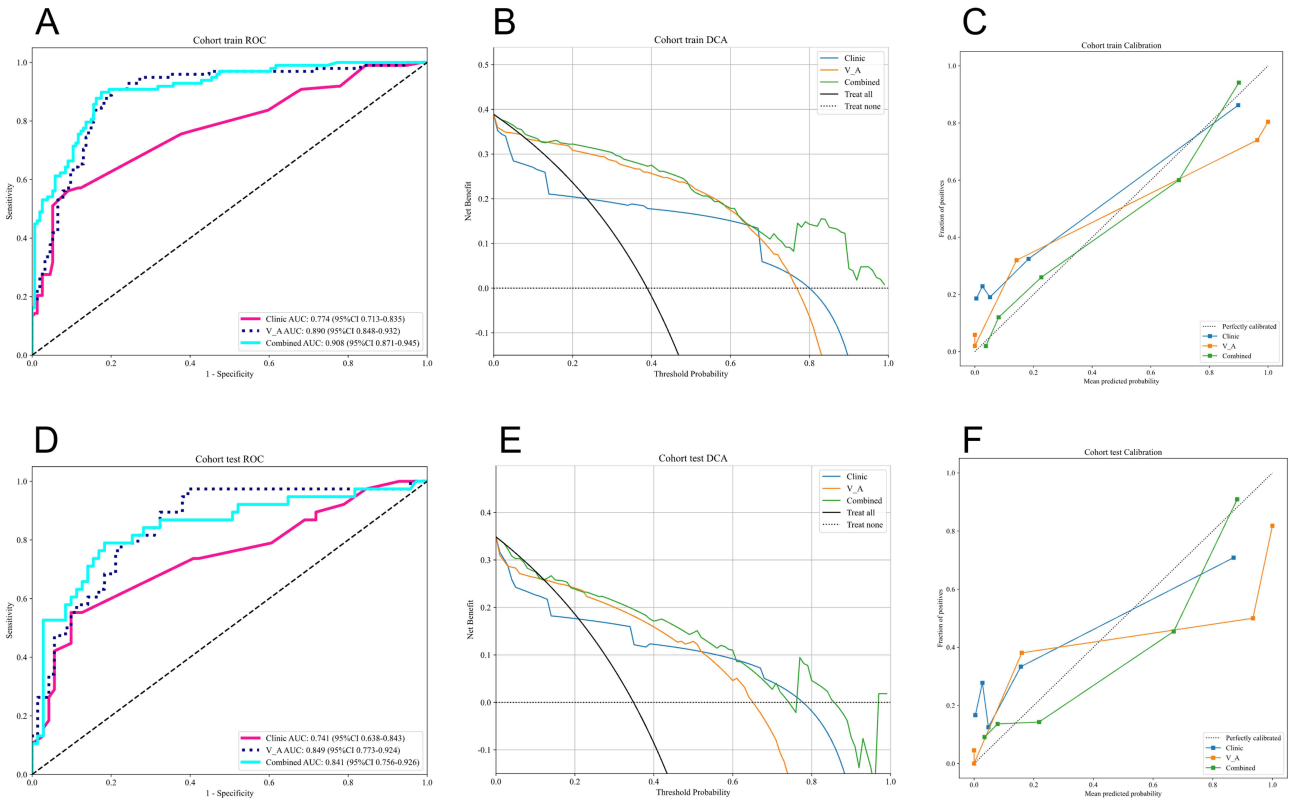

Figure 6 ROC, DCA, and calibration curves for the clinical, radiomics, and combined models in the training set (**A**–**C**) and test set (**D**–**F**). V-A represents the AP and PVP fusion model of Intra-peri 5mm.
Abbreviations: ROC, receiver operating characteristics; DCA, decision curve analysis.

Discussion

The invasiveness of tumors is a key determinant in clinical decision-making and a principal prognostic indicator in HCC. In this study, we evaluated the preoperative predictive utility of three distinct peritumoral ranges (peri-3 mm, peri-5 mm, and peri-10 mm) for PHCC. The findings indicated that a combined model incorporating intratumoral and 5-mm peritumoral features provided superior performance in predicting PHCC.

Our findings also revealed heterogeneous enhancement patterns in PHCC during AP and PVP. Aggressive vascular patterns, including MVI and vessels encapsulating tumor clusters (VETC), correlate with poor clinical outcomes.[22] The MTM-HCC subtype comprised the majority of PHCC cases (56.6%) in our cohort. Its coarse trabecular architecture and rapid growth pattern result in intratumoral hypoperfusion and necrosis, which manifests as hypodense regions on CT imaging with focal arterial hypoenhancement (Figure 8).[23] PHCC is generally associated with irregular angiogenesis, necrosis, and stromal heterogeneity. Consistently, as shown in Figure 5, the top feature in the SHAP Waterfall Plot (peri_exponential_glszm_GrayLevelNonUniformity_V) reflects the uneven distribution of isointense voxel regions in the peritumoral area after exponential transformation. A higher value indicates an increase in peritumoral heterogeneity. This suggests that the increased gray level non-uniformity of the texture in the peritumoral tissue may be associated with HCC that is more invasive or prone to recurrence.

Although conventional radiomics primarily focuses on intratumoral features,[24] high-grade tumors also display peritumoral signatures, including capsular disruption and heterogeneous enhancement. Yu et al demonstrated the superior predictive value of peritumoral radiomic features for VETC identification using gadoxetic acid-enhanced MRI.[25]

The tumor microenvironment (TME) plays a pivotal role in tumorigenesis, progression, and metastasis. The extracellular matrix releases diverse factors that drive hypoxia and angiogenesis—key determinants of tumor biological behavior.[26] Since TME characteristics vary widely among patients (for example, hypoxia gradients, immune contexture), personalized characterization is essential. Meng et al pioneered the use of functional CT nanoprobes to map tumor

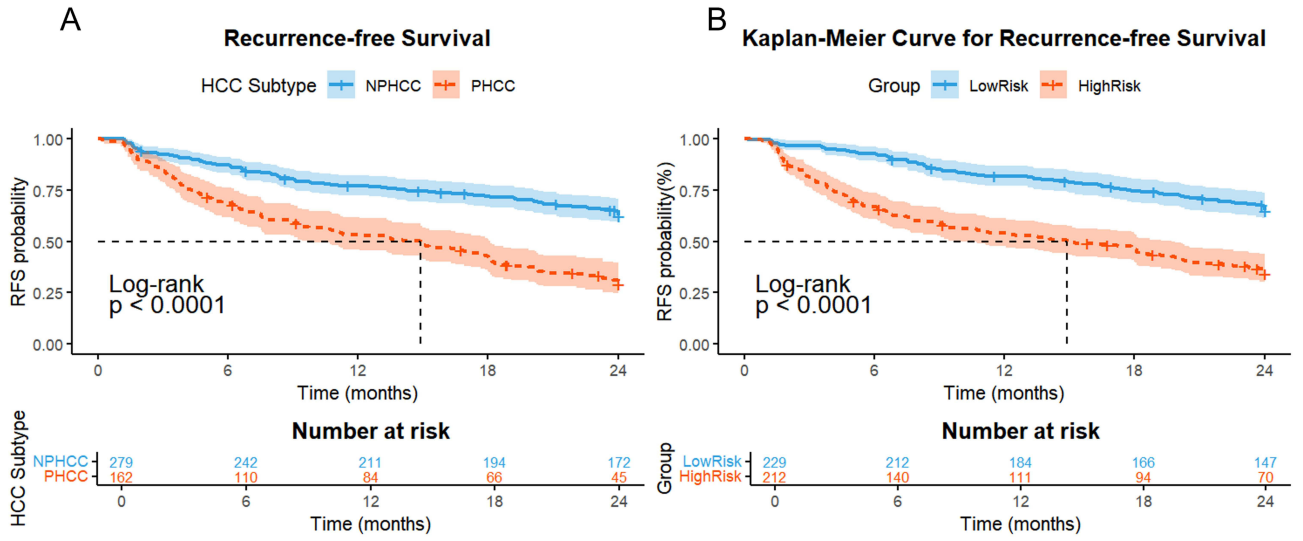

Figure 7 Kaplan–Meier analysis of RFS. (**A**) PHCC vs NPHCC. (**B**) High-risk vs low-risk groups.
Abbreviations: RFS, recurrence-free survival; PHCC, proliferative hepatocellular carcinoma; NPHCC, non-proliferative hepatocellular carcinoma.

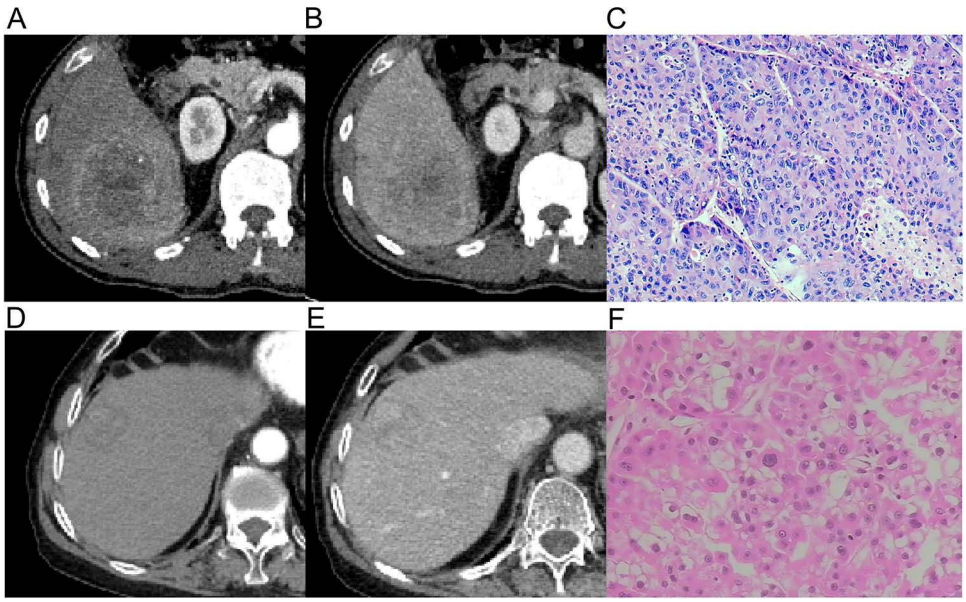

Figure 8 Representative CT and pathological images of PHCC and NPHCC. (**A**–**C**) PHCC: MTM-HCC subtype, male, 58 years old. The tumor shows a blurred boundary with an incomplete capsule and extensive intratumoral necrosis. Heterogeneous AP enhancement with intralesional vessels is visible (RFS = 19.2 months). (**D**–**F**) NPHCC: Clear cell subtype, female, 70 years old. The tumor has a well-defined boundary, shows AP enhancement, and maintains enhancement in the PVP. No postoperative recurrence occurred.
Abbreviations: CT, computed tomography; PHCC, proliferative hepatocellular carcinoma; NPHCC, non-proliferative hepatocellular carcinoma; MTM-HCC, macrotrabecular-massive hepatocellular carcinoma; AP, arterial phase; RFS, recurrence-free survival; PVP, portal venous phase.

hypoxia, offering innovative diagnostic and therapeutic strategies.[27] These nanoprobes enhance drug delivery within tumor tissue while minimizing off-target toxicity, especially for aggressive or treatment-resistant tumors. Integrating intratumoral and peritumoral data enables a more comprehensive assessment of invasion and metastasis patterns. Building on this concept, subsequent studies have systematically evaluated optimal peritumoral sampling margins.[28,29] Zhao et al found that a 3-mm peritumoral region (AUC = 0.911; 95% CI: 0.825–0.975) better predicted HCC response to TACE than 5-mm (AUC = 0.909; 95% CI: 0.817–0.982) or 10-mm (AUC = 0.895, 95% CI: 0.815–0.964) regions. In our

study, however, the 5-mm zone achieved the highest performance in differentiating PHCC subtypes (AUC = 0.839 vs 0.748 for 3 mm and 0.768 for 10 mm). We hypothesize that the 5-mm peritumoral region encompasses biologically informative features—such as MVI density; in contrast, larger margins (for example, 10 mm) introduce confounding signals from adjacent normal parenchyma, reducing predictive accuracy.

Targeting the TME remains a promising approach for improving prognosis and treatment outcomes in HCC. Anti-angiogenic agents such as sorafenib can suppress neovascularization and proliferation by inhibiting VEGF receptors and RAF kinase signaling.[30] Combining PD-1 inhibitors with VEGF inhibitors has also shown synergistic effects in remodeling the TME.[31] Although these advances are transforming systemic therapy for advanced HCC, their therapeutic implications in this context should be considered exploratory and require validation in future translational and prospective studies.

Our study further showed that radiomics-predicted PHCC subtypes exhibited significantly higher early recurrence rates than NPHCC subtypes ($p < 0.001$), suggesting proliferative activity may serve as an independent biomarker for immunotherapy stratification. Noninvasive imaging characterization of the TME may therefore provide a platform for developing novel combinatorial strategies that simultaneously block oncogenic drivers and resensitize treatment-resistant tumors, enabling precision therapy selection.

Medical imaging modalities, particularly CT and MRI, remain essential for diagnosing and monitoring HCC. In this study, radiological models provided more effective preoperative risk stratification than conventional approaches. CT remains the preferred modality before and after surgery because of its rapid acquisition and superior contrast resolution. However, while CT effectively delineates tumor morphology, size, and enhancement patterns, it lacks standardized quantitative biomarkers for tissue heterogeneity. Radiomics addresses this limitation by extracting spatiotemporal features of tumor vascular perfusion from imaging data, allowing noninvasive prediction of biological aggressiveness. This approach not only informs personalized treatment strategies but also establishes a robust framework for prognostic stratification.

Limitations

First, as an inherent limitation of retrospective designs, our analysis is susceptible to selection bias and may therefore constrain the strength of causal inference. Second, despite our efforts in image normalization, the observed variability in CT acquisition protocols (eg, reconstruction kernels and tube current) across different centers likely introduced non-biological variance into the radiomics features. Third, although a 5mm boundary was used to optimally capture the tumor microenvironment signals, there is a lack of unified consensus in radiomics regarding the optimal margin. Its spatial universality requires further validation using varying margin specifications. Fourth, a crucial limitation is the inherent lack of direct mechanistic insight provided by radiomics features. Being complex mathematical transformations of pixel data, these features primarily capture phenomenological descriptions of tumor heterogeneity, and their direct biological interpretability is constrained. Future research is warranted to correlate these signatures with genomic or proteomic data to establish a robust biological foundation.

Conclusion

In this study, we developed a novel radiomics model that integrates multi-phase (AP and PVP) intra- and peritumoral features to non-invasively predict PHCC. We identified that a 5-mm peritumoral margin most effectively captures tumor microenvironmental signals critical for prediction. The model's robustness was demonstrated through its strong performance in an external validation cohort, while the inclusion of SHAP analysis provided clear interpretability, revealing that peritumoral texture features in the PVP phase were the most influential factors in predicting PHCC subtypes. Clinically, this model offers a valuable non-invasive tool for preoperative patient stratification, enabling clinicians to accurately identify high-risk patients who may benefit from more aggressive or tailored treatment approaches, such as neoadjuvant therapy or enhanced postoperative surveillance. Future work should aim to validate these findings across diverse populations and integrate multi-omics data to develop a comprehensive prognostic system.

Data Sharing Statement

All relevant data are available within the manuscript. Further enquiries can be directed to the corresponding author.

Ethics Approval and Informed Consent

This retrospective study was approved by the Ethics Committee of the First Affiliated Hospital of Guangxi Medical University (Approval No. 2025-E0431) and the Ethics Committee of Guangxi Medical University Cancer Hospital (Approval No. KY2025984). The requirement for written informed consent was waived, and the study was conducted in full accordance with the Declaration of Helsinki. In the processes of data collection, storage, and analysis, we implemented stringent privacy protection measures, including data de-identification and encrypted storage, to ensure that participant privacy is not compromised. The results of this study are presented only in aggregated form and do not include any personally identifiable information.

Acknowledgement

We generally thank the Department of Medical Imaging Center, GuangxiMedical University Cancer Hospital for their assistance in data acquisition and support as the second study center.

Author Contributions

All authors made a significant contribution to the work reported, whether that is in the conception, study design, execution, acquisition of data, analysis and interpretation, or in all these areas; took part in drafting, revising or critically reviewing the article; gave final approval of the version to be published; have agreed on the journal to which the article has been submitted; and agree to be accountable for all aspects of the work.

Funding

The study was partially support by National Natural Science Foundation of China (82060310).

Disclosure

The authors report no conflicts of interest in this work.

References

1. Bray F, Laversanne M, Sung H, et al. Global cancer statistics 2022: GLOBOCAN estimates of incidence and mortality worldwide for 36 cancers in 185 countries. *CA Cancer J Clin*. 2024;74(3):229–263. doi:10.3322/caac.21834
2. World Health Organization. *WHO Classification of Tumours: Digestive System Tumours*. 5th ed. Lyon: International Agency for Research on Cancer (IARC); 2019.
3. Krinsky G, Shanbhogue K. Proliferative versus nonproliferative hepatocellular carcinoma: clinical and imaging implications. *Radiology*. 2021;300 (3):583–585. doi:10.1148/radiol.2021211316
4. Huang SC, Liao SH, Su TH, Jeng YM, Kao JH. Clinical manifestations and outcomes of patients with scirrhous hepatocellular carcinoma. *Hepatol Int*. 2021;15(2):472–481. doi:10.1007/s12072-021-10146-1
5. Ziol M, Poté N, Amaddeo G, et al. Macrotrabecular-massive hepatocellular carcinoma: a distinctive histological subtype with clinical relevance. *Hepatology*. 2018;68(1):103–112. doi:10.1002/hep.29762
6. Zeng J, Zeng J, Lin K, et al. Development of a machine learning model to predict early recurrence for hepatocellular carcinoma after curative resection. *Hepatobiliary Surg Nutr*. 2022;11(2):176–187. doi:10.21037/hbsn-20-466
7. Zhou SL, Zhou ZJ, Song CL, et al. Whole-genome sequencing reveals the evolutionary trajectory of HBV-related hepatocellular carcinoma early recurrence. *Signal Transduct Target Ther*. 2022;7(1):24. doi:10.1038/s41392-021-00838-3
8. Yan H, Liu L, Wang D, et al. Microinvasion in hepatocellular carcinoma: predictive factor and application for definition of clinical target volume for radiotherapy. *World J Surg Oncol*. 2024;22(1):125. doi:10.1186/s12957-024-03399-1
9. Wang F, Cheng M, Du B, et al. Predicting microvascular invasion in small (≤5 cm) hepatocellular carcinomas using radiomics-based peritumoral analysis. *Insights Imaging*. 2024;15(1):90. doi:10.1186/s13244-024-01649-0
10. Liu HF, Wang M, Wang Q, et al. Multiparametric MRI-based intratumoral and peritumoral radiomics for predicting the pathological differentiation of hepatocellular carcinoma. *Insights Imaging*. 2024;15(1):97. doi:10.1186/s13244-024-01623-w
11. Han L, Lin X, Yan Q, et al. PBLD inhibits angiogenesis via impeding VEGF/VEGFR2-mediated microenvironmental cross-talk between HCC cells and endothelial cells. *Oncogene*. 2022;41(13):1851–1865. doi:10.1038/s41388-022-02197-x
12. Dal Bo M, De Mattia E, Baboci L, et al. New insights into the pharmacological, immunological, and CAR-T-cell approaches in the treatment of hepatocellular carcinoma. *Drug Resist Updat*. 2020;51:100702. doi:10.1016/j.drup.2020.100702

13. Marron TU, Fiel MI, Hamon P, et al. Neoadjuvant cemiplimab for resectable hepatocellular carcinoma: a single-arm, open-label, Phase 2 trial. *Lancet Gastroenterol Hepatol*. 2022;7(3):219–229. doi:10.1016/S2468-1253(21)00385-X
14. Llovet JM, Castet F, Heikenwalder M, et al. Immunotherapies for hepatocellular carcinoma. *Nat Rev Clin Oncol*. 2022;19(3):151–172. doi:10.1038/s41571-021-00573-2
15. Feng Z, Li H, Zhao H, et al. Preoperative CT for characterization of aggressive macrotrabecular-massive subtype and vessels that encapsulate tumor clusters pattern in hepatocellular carcinoma. *Radiology*. 2021;300(1):219–229. doi:10.1148/radiol.2021203614
16. Lambin P, Leijenaar RTH, Deist TM, et al. Radiomics: the bridge between medical imaging and personalized medicine. *Nat Rev Clin Oncol*. 2017;14(12):749–762. doi:10.1038/nrclinonc.2017.141
17. Xu Y, Zhou C, He X, et al. Deep learning-assisted LI-RADS grading and distinguishing hepatocellular carcinoma (HCC) from non-HCC based on multiphase CT: a two-center study. *Eur Radiol*. 2023;33(12):8879–8888. doi:10.1007/s00330-023-09857-w
18. Kang HJ, Kim H, Lee DH, et al. Gadoxetate-enhanced MRI features of proliferative hepatocellular carcinoma are prognostic after surgery. *Radiology*. 2021;300(3):572–582. doi:10.1148/radiol.2021204352
19. Zhang W, Li N, Li J, et al. Noninvasive identification of proliferative hepatocellular carcinoma on multiphase dynamic CT: quantitative and LI-RADS lexicon-based evaluation. *Eur Radiol*. 2025;35(6):3460–3475. doi:10.1007/s00330-024-11247-9
20. Shin J, Seo N, Baek SE, et al. MRI radiomics model predicts pathologic complete response of rectal cancer following chemoradiotherapy. *Radiology*. 2022;303(2):351–358. doi:10.1148/radiol.211986
21. Peduzzi P, Concato J, Kemper E, Holford TR, Feinstein AR. A simulation study of the number of events per variable in logistic regression analysis. *J Clin Epidemiol*. 1996;49(12):1373–1379. doi:10.1016/s0895-4356(96)00236-3
22. Meng XP, Tang TY, Zhou Y, et al. Predicting post-resection recurrence by integrating imaging-based surrogates of distinct vascular patterns of hepatocellular carcinoma. *JHEP Rep*. 2023;5(9):100806. doi:10.1016/j.jhepr.2023.100806
23. Rhee H, Cho ES, Nahm JH, et al. Gadoxetic acid-enhanced MRI of macrotrabecular-massive hepatocellular carcinoma and its prognostic implications. *J Hepatol*. 2021;74(1):109–121. doi:10.1016/j.jhep.2020.08.013
24. Feng Z, Li H, Liu Q, et al. CT radiomics to predict macrotrabecular-massive subtype and immune status in hepatocellular carcinoma. *Radiology*. 2023;307(1):e221291. doi:10.1148/radiol.221291
25. Yu Y, Fan Y, Wang X, et al. Gd-EOB-DTPA-enhanced MRI radiomics to predict vessels encapsulating tumor clusters (VETC) and patient prognosis in hepatocellular carcinoma. *Eur Radiol*. 2022;32(2):959–970. doi:10.1007/s00330-021-08250-9
26. Xiao Y, Hassani M, Moghaddam MB, Fazilat A, Ojarudi M, Valilo M. Contribution of tumor microenvironment (TME) to tumor apoptosis, angiogenesis, metastasis, and drug resistance. *Med Oncol*. 2025;42(4):108. doi:10.1007/s12032-025-02675-8
27. Meng X, Wu Y, Bu W. Functional CT contrast nanoagents for the tumor microenvironment. *Adv Healthc Mater*. 2021;10(5):e2000912. doi:10.1002/adhm.202000912
28. Liu W, Li L, Deng J, Li W. A comprehensive approach for evaluating lymphovascular invasion in invasive breast cancer: leveraging multimodal MRI findings, radiomics, and deep learning analysis of intra- and peritumoral regions. *Comput Med Imag Graph*. 2024;116:102415. doi:10.1016/j.compmedimag.2024.102415
29. Wang XX, Ding Y, Wang SW, et al. Intratumoral and peritumoral radiomics analysis for preoperative Lauren classification in gastric cancer. *Cancer Imag*. 2020;20(1):83. doi:10.1186/s40644-020-00358-3
30. Zhu AX, Finn RS, Edeline J, et al. Pembrolizumab in patients with advanced hepatocellular carcinoma previously treated with sorafenib (KEYNOTE-224): a non-randomised, open-label phase 2 trial. *Lancet Oncol*. 2018;19(7):940–952. doi:10.1016/S1470-2045(18)30351-6
31. Zhou Z, Li X, Yang G, et al. Targeting β-catenin and PD-L1 simultaneously by a racemic supramolecular peptide for the potent immunotherapy of hepatocellular carcinoma. *Theranostics*. 2023;13(10):3371–3386. doi:10.7150/thno.83377